Journal of Industrial and Engineering Chemistry 81 (2020) 61–66

Contents lists available at ScienceDirect

Journal of Industrial and Engineering Chemistry

journal homepage: www.elsevier.com/locate/jiec

High-performance nanohybrid anode based on FeS_2 nanocubes and nitrogen-rich graphene oxide nanoribbons for sodium ion batteries

Jaewon Choi[a], Seung Uk Yoon[b], Min Eui Lee[c], Seong In Park[c], Yoon Myung[d], Hyoung-Joon Jin[b], Jin Bae Lee[e,**], Young Soo Yun[f,g,*]

[a] Department of Chemistry and Research Institute of Natural Sciences, Gyeongsang National University, Jinju 52828, South Korea
[b] Department of Polymer Science and Engineering, Inha University, Incheon 22212, South Korea
[c] Institute of Advanced Composite Materials, Korea Institute of Science and Technology, 92 Chudong-ro, Bongdong-eup, Wanju-gun, Jeonbuk 55324, South Korea
[d] Korea Institute of Industrial Technology, Dongnam Regional Division, Busan 46744, South Korea
[e] Korea Basic Science Institute, Daejeon 34133, South Korea
[f] Department of Chemical Engineering, Kangwon National University, Samcheok 25913, South Korea
[g] KU-KIST Graduate School of Converging Science and Technology, Korea University, Seoul 02841, South Korea

ARTICLE INFO

Article history:
Received 9 July 2019
Received in revised form 22 August 2019
Accepted 27 August 2019
Available online 30 August 2019

Keywords:
Iron disulfide
Graphene nanoribbon
Sodium ion batteries
Nanohybrid
Anode

ABSTRACT

Sodium ion batteries (SIBs) have attracted considerable attention as an alternative to Li ion batteries (LIBs) because of the sustainable sodium resources and similar chemistry to LIBs. On the other hand, the larger and heavier sodium results in unfavorable sodium ion storage capacity. In this study, an inexpensive precursor-based conversion material, FeS_2, was synthesized as a nanostructured pyrite crystal, <100 nm in size, which has a carbon coating layer, a few nanometers in thickness. The deficient electrical conductivity of the synthesized FeS_2 nanocubes (FeS_2-NCs) was strengthened by forming a nanohybrid structure with high-aspect ratio graphene oxide nanoribbons containing nitrogen dopants (N-GONRs). N-GONRs bind tightly the FeS_2-NCs well-dispersed in the N-GONRs matrix, inducing highly improved electrochemical performance as an anode for SIBs. The FeS_2-NCs/N-GONRs nanohybrid anode delivered a high reversible capacity of ~800 mA h g^{-1} at 0.2 A g^{-1}, of which approximately 60% was maintained at a 50 times higher current rate, indicating high rate capability. In addition, stable cycling performance over 200 cycles was achieved with an average capacity of ~670 mA h g^{-1}. The hybrid anode demonstrated its feasibility in a full cell test using an O_3-type cathode material.

Introduction

Sodium ion batteries (SIBs) are noteworthy power sources for large scale energy storage owing to the natural abundance of sodium as well as the technological similarity to the widely used lithium ion battery (LIB) [1–3]. A key issue with SIBs is how much their energy density can be improved compared to LIBs because sodium has relatively unfavorable intrinsic properties; sodium is not only several times larger and heavier, but also has a 0.33 eV higher electrode potential [1–4]. The energy density is normally determined by the active electrode materials (AEMs), which store charges by intercalation, conversion reactions, and/or alloying reaction(s) [5]. Intercalation-based AEMs allow charges to be inserted in an equivalent site of a given crystal lattice with the formation of a new crystal phase [1,2,6]. This means that conventional intercalation-based chemistry is not an option for SIBs owing to the disadvantageous properties of sodium. In contrast, conversion reaction-based AEMs (CR-AEMs), such as SnO_2 [7], CuS [8,9], SnS [10,11], FeS_2 [12–15], and SnP_3 [16], with high theoretical capacities of ~1100 mA h g^{-1} can deliver much higher energies as an anode, when a well-designed nanostructure and conducting pathway are applied. In particular, the low cost and mass-scalability of FeS_2 highlight its high potential as a high energy anode material for SIBs [12–15]. Zhu et al. reported that in an ether-based electrolyte, FeS_2 can deliver a specific capacity of ~640 mA h g^{-1} at a current of 20 mA g^{-1}, of which specific capacities, corresponding to 290 and 415 mA h g^{-1}, were maintained at an increased current rate of 200 mA g^{-1} and after 100 cycles, respectively [12]. Walter et al. reported that a nanostructured FeS_2 show improved rate and cycling performance [13]. In

* Corresponding author at: Graduate School of Converging Science and Technology, Korea University, Seoul 02841, South Korea
** Corresponding author.
E-mail addresses: jblee@kbsi.re.kr (J.B. Lee), ysyun@kangwon.ac.kr (Y.S. Yun).

https://doi.org/10.1016/j.jiec.2019.08.059
1226-086X/

addition, FeS_2/carbon nanocomposites achieved even better cycling performance [14]. These results suggest that practicable CR-AEMs can be developed through sophisticated electrode design using state-of-the-art carbon nanomaterials.

A graphene nanoribbon (GNR) is a poly-aromatic sp^2-carbon strip with a high aspect ratio and good electrical conductivity [17,18]. Its high specific surface area and numerous edge sites can provide a large number of active sites for sodium ion storage [19–21], which can be maximized when a chemical synthetic method via a strong acid treatment is used for its production. Carbon nanotubes (CNTs) can be unzipped through the fiber-axis through wet chemistry, resulting in highly oxidized GNRs (GONRs) with high aspect ratios [22]. After a chemical reduction process using hydrazine, the GONRs can be transformed to chemically reduced GONRs, including nitrogen heteroatoms (N-rGONRs) [23]. Because N-rGONRs have additional redox-active sites as well as increased electrical conductivities with electron doping, they can provide CR-AEMs with a well-developed conducting network that is helpful for the overall capacities [19,24]. Moreover, the morphological uniqueness with a high aspect ratio and specific surface area can bind the respective FeS_2 nanoparticles, resulting in stable cycling behaviors [25].

In this study, FeS_2 nanocubes (FeS_2-NCs) and N-rGONRs were prepared using a wet process, and hybridized through simple vacuum filtration. In the nanohybrids, the FeS_2-NCs were bound thoroughly by N-rGONR networks, showing noticeable sodium ion storage performance. The FeS_2-NC/N-GONR nanohybrid anode could deliver a reversible capacity of ~800 mA h g^{-1} at 0.2 A g^{-1}, and approximately 60% of the initial capacity was maintained at a 50 times higher current rate. The initial capacity was also well-maintained after 200 consecutive cycles. Moreover, the feasible electrochemical performance of the nanohybrid anode was demonstrated through a full cell test using an O_3-type cathode material.

Experimental

Preparation of FeS_2-NCs, N-GONRs and FeS_2-NCs/N-GONRs nanohybrid anode

FeS_2-NCs were synthesized in 50 ml three-neck Schlenk flask under an Ar atmosphere. Oleyamine (15 ml, 70%, Aldrich) was injected into the flask and vacuum-dried with 800 rpm stirring at 120 °C. Sulfur (96.2 mg, 99.998%, Aldrich), 1,2-dodecanediol (101.2 mg, >93.0%, TCI) and $FeCl_2$ (63.4 mg, 99.5%, Alfa Aesar) were added to the flask. The mixture solution was then reacted for 6 h with stirring at 800 rpm under an Ar atmosphere. After the synthetic process, the reaction flask was cooled to room temperature and washed with 10 ml of ethanol (94.5%, Daejung) and 20 ml of *n*-hexane (95%, Daejung) by centrifugation. The resulting products were treated thermally in a tubular furnace at 400 °C for 2 h under an Ar atmosphere. The as-prepared FeS_2-NCs were stored in a vacuum oven at 30 °C.

The N-GONRs were prepared by unzipping CNTs (95%, Hanwha Nanotech) by a strong acid treatment. A 200 mg sample of CNTs was immersed in sulfuric acid (95%, Daejung) for 12 h at room temperature, which was followed by the addition of 1000 mg of $KMnO_4$ (99.0%, Aldrich). The mixture solution was stirred at room temperature for 1 h, and heated to 60 °C for an additional 1 h. The reaction mixture was poured into 400 ml of ice containing 50 ml of 30% H_2O_2. The solution was vacuum-filtered and washed several times with distilled water. The resulting products were dispersed in *N,N*-dimethylformamide (DMF, 99.8% Daejung) by an ultrasound treatment and reacted with hydrazine (~1 ml, 35%, Aldrich). The N-GONR dispersions (0.1 wt.%) were obtained after the fabrication process.

A 12 mg sample of FeS_2-NCs was dispersed in the N-GONR (8 mg) dispersion by an ultrasound treatment for 10 min, and the mixture solution was then vacuum-filtered in an Anodisk membrane filter (47 mm diameter, 0.2 μm pores, Whatman). The FeS_2-NCs/N-GONR nanohybrid anode was finally obtained after vacuum drying at 30 °C for 12 h.

Characterization

The morphologies of the FeS_2-NCs and FeS_2-NCs/N-GONRs nanohybrids were observed by field emission scanning electron microscopy (FE-SEM) with energy dispersive spectroscopy (EDS, S-4300SE, Hitachi, Japan) and field emission transmission electron microscopy (FE-TEM, JEM2100F, JEOL, Japan). X-ray diffraction (XRD, Rigaku, DMAX 2500) was conducted using a Cu Kα radiation (λ = 0.154 nm) at 40 kV and 100 mA over the range, 5–60° 2θ. The Raman spectrum was recorded using a continuous-wave linearly polarized laser (514.5 nm, 2.41 eV, 16 mW). The laser beam was

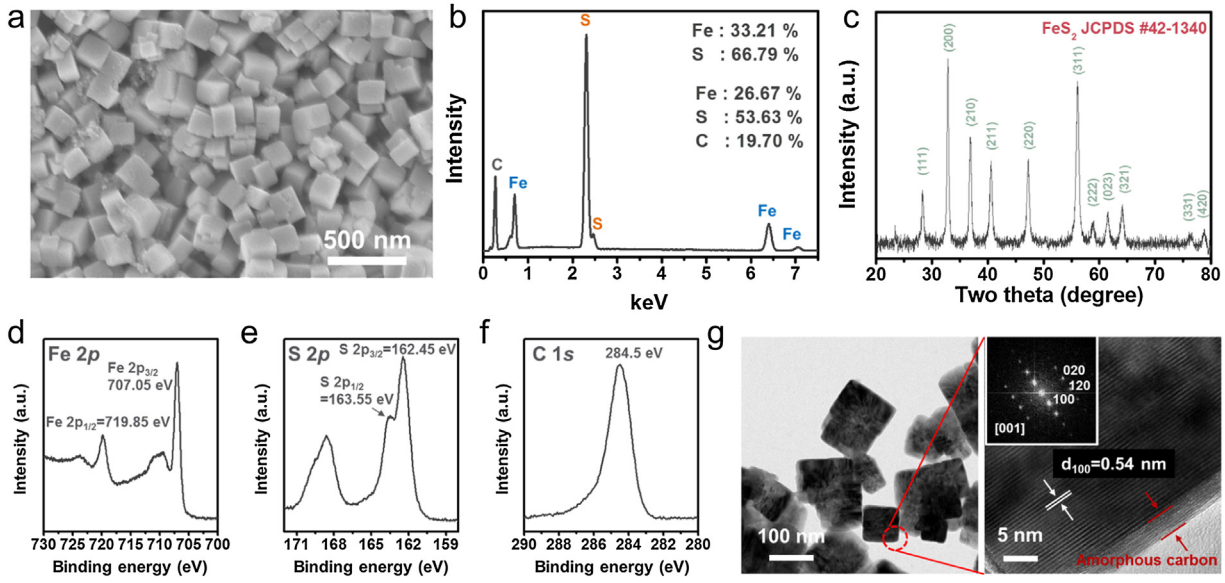

Fig. 1. Material properties of FeS_2-NCs: (a) FE-SEM image, (b) EDS data, (c) XRD pattern, XPS (d) Fe 2*p*, (e) S 2*P* and (f) C 1*s* spectra, and (g) FE-TEM images (Inset of selective area diffraction pattern).

focused using a 100× objective lens, resulting in a 1-μm diameter spot. The acquisition time and number of cycles for the collection of each spectrum were 10 s and 3, respectively. The chemical composition and depth profile of the samples were examined by X-ray photoelectron spectroscopy (XPS, PHI 5700 ESCA, Chanhassen, USA) using monochromatic Al Kα radiation.

Electrochemical characterization

The electrochemical properties of the FeS_2-NCs, FeS_2-NCs/N-GONRs nanohybrids, and $[Li_{0.05}(Ni_{0.25}Fe_{0.25}Mn_{0.5})_{0.95}]O_2$ cathode were examined using a Wonatech automatic battery cycler and CR2032-type coin cells. For the half-cell experiments, coin cells were assembled in a glovebox filled with argon using them as the working electrode and metallic Na foil as the reference and counter electrodes. $NaPF_6$ (1 M; Sigma-Aldrich, 98%) was dissolved in a solution of diethylene glycol dimethyl ether (DEGDME) and used as the electrolyte. A glass microfiber filter (GF/F, Whatman) was used as the separator. The working electrodes were prepared by mechanically producing working electrode cylinders, 1/2 in. in diameter. For the cathode, the working electrodes were prepared by mixing the active material (70 wt.%) with conductive carbon (20 wt.%) and polyvinylidene fluoride (10 wt.%) in *N*-methyl-2-pyrrolidone. The resulting slurries were applied uniformly to Al foil. The electrodes were dried at 120 °C for 2 h and roll pressed.

Results and discussion

As-prepared FeS_2-NCs had a cubic morphology with a particle size of <100 nm (Figs. 1(a) and S1). EDS revealed a stoichiometric Fe atomic ratio (Fe/S) of 0.5:1 (Fig. 1(b)), showing that pure FeS_2-NCs had been fabricated. In the XRD patterns, several sharp peaks corresponding to a pyrite FeS_2 structure were confirmed (Fig. 1(c)). The XPS Fe 2*p* and S 2*p* spectra revealed the characteristic bonding of FeS_2 (Fig. 1(d,e)). One noticeable result is the presence of carbon atoms. The XPS C 1*s* spectrum exhibited sp^2 C=C bonding at 284.5 eV (Fig. 1(f)). The C/S atomic ratio in the XPS spectra was 0.56, suggesting that carbon compounds were present on the surface of the FeS_2-NCs. The surface carbon structure was confirmed by high resolution FE-TEM, as shown in Fig. 1(g). An amorphous carbon layer, a few nanometers in size was coated homogeneously on the surface of the FeS_2-NCs (Fig. 1(g)), and the inner bulk material had a highly ordered crystal structure with a lattice distance of ~0.54 nm, corresponding to the pyrite (100) lattice (Fig. 1(g)). These results suggest that FeS_2-NCs have a core-shell nanostructure composed of an amorphous carbon thin layer shell and a well-ordered FeS_2 core. The surface carbon layer could increase electrical conductivity of the respective FeS_2-NCs and be helpful in producing a stable solid-electrolyte-interface (SEI) layer, resulting in improved cycling performance.

The FeS_2-NCs were dispersed in an organic solvent, DMF, which is a good solvent for carbon-based materials [26,27], and mixed with an N-rGONR dispersion in the same solvent. The mixture solution, including FeS_2-NCs and N-rGONRs, were vacuum-filtered, resulting in homogeneously scattered FeS_2-NCs, which were bound by N-rGONRs networks (Fig. 2(a,b)). The N-rGONRs were a few nanometers in thickness with a significantly long length (aspect ratio of >100) (Fig. 2(b)), and had a large number of topological defects, as shown in the high-resolution FE-TEM image (Fig. 2(c)). The carbon microstructure of the N-rGONRs was characterized further by Raman spectroscopy, in which clear *D* and *G* bands were observed (Fig. 2(d)). The *D* band comes from the disordered A_{1g} breathing mode of the cyclic carbon structures, whereas the *G* band arises from the E_{2g} vibration mode of poly-hexagonal carbon structures [28]. The presence of both *D* and *G* bands indicates that the poly-cyclic carbon structures are well-developed. The *D* to *G* intensity ratio (I_D/I_G) was 1.34, suggesting that the N-rGONRs have poly-conjugated carbon domains on the scale of a few nanometers. The chemical structure of N-rGONRs was investigated by XPS (Fig. 2(e–g)). In the XPS C 1*s* spectrum, the peak for the C=C bond was found at 284.3 eV, and those for sp^3 C—C, C—O and C—N, and C=O bonds were observed at 284.7, 286.3 and 288.6 eV, respectively (Fig. 2(e)) [29]. The oxygen groups were composed of C=O and C—O bonds at 531.3 and 532.9 eV, respectively (Fig. 2(f)). In addition, nitrogen functional groups were confirmed to have three different chemical structures, such as pyridinic-N, pyridonic-N, and N-oxide centered at 399.5, 401.4, and 402.8 eV, respectively (Fig. 2(g)) [29]. The polar functional groups enable N-rGONRs to have good wettability for the glyme-based

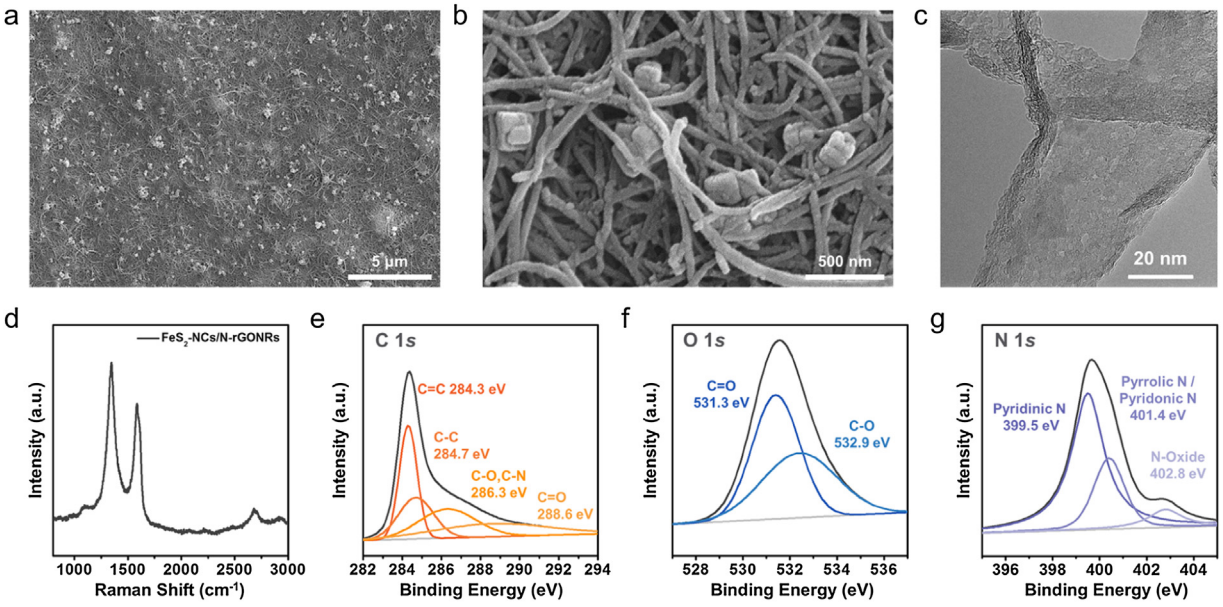

Fig. 2. Material properties of the FeS_2-NCs/N-GONRs nanohybrid anode: (a, b) FE-SEM images at different magnifications, (c) FE-TEM image, (d) Raman spectrum, and XPS (e) C 1s, (f) O 1s and (g) N 1s spectra.

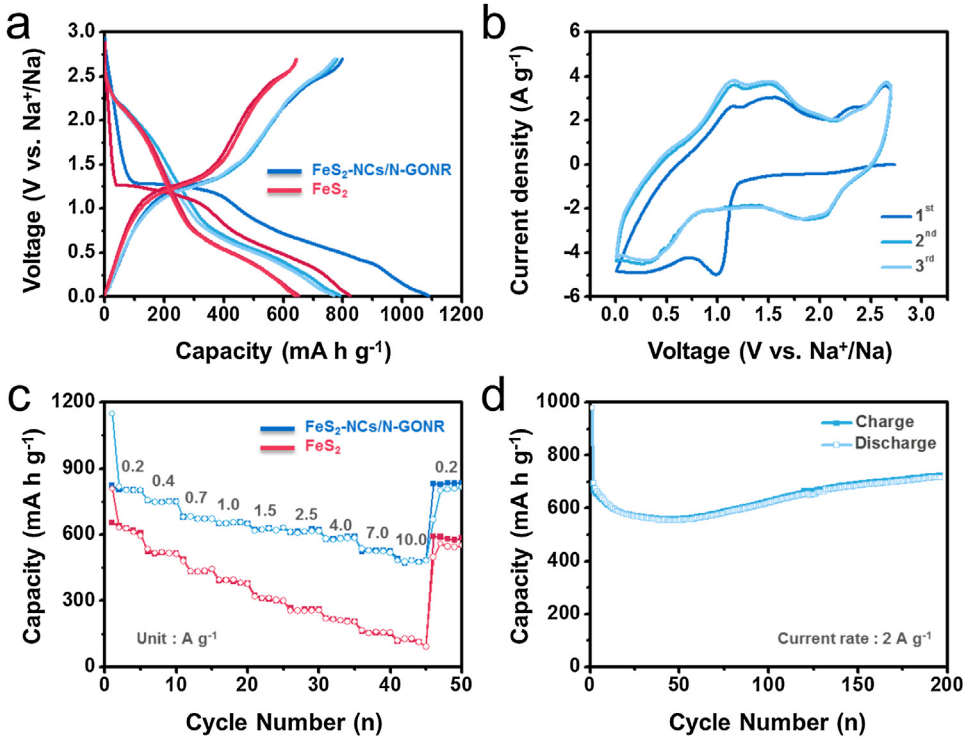

Fig. 3. Electrochemical performance of the FeS_2-NCs anode and FeS_2-NCs/N-GONRs hybrid anode characterized in an electrolyte of 1 M $NaPF_6$ dissolved in DEGDME over a voltage window of 0.01–2.7 V vs. Na^+/Na. (a) Galvanostatic discharge/charge profiles of both anodes at a current rate of 0.2 A g^{-1}, (b) CV curves of the nanohybrid anode at a scan rate of 0.01 mV s^{-1}, (c) rate capabilities of both anodes in different current densities from 0.2 to 10 A g^{-1}, and (d) cycling performance of the hybrid anode during 200 cycles characterized at 2 A g^{-1}.

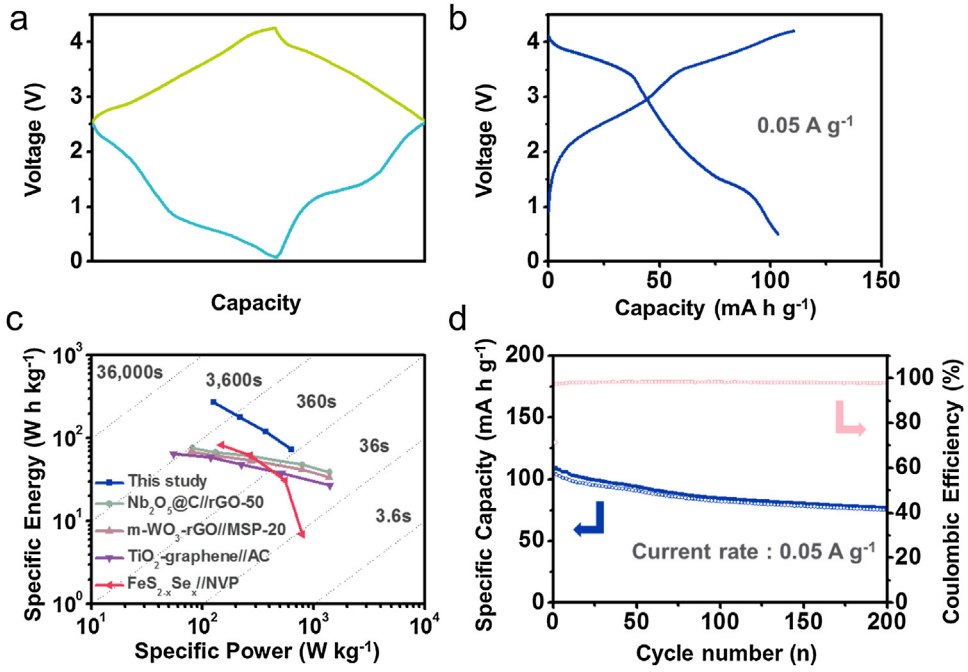

Fig. 4. Electrochemical performance of a full cell composed of FeS2-NCs/N-GONRs//$Na_{0.9}$ + $[Li_{0.05}(Ni_{0.25}Fe_{0.25}Mn_{0.5})_{0.95}]O_2$ in an electrolyte of 1 M $NaPF_6$ dissolved in DEGDME over a voltage window of 1.0–4.2 V. (a) Schematic diagram of galvanostatic charge/discharge profiles of both the anode and cathode, (b) galvanostatic charge/discharge profile of the full cell at a current rate of 0.05 A g^{-1}, (c) Ragone plots of several energy storage devices, including FeS_2-NCs/N-GONRs//$Na_{0.9}$ + $[Li_{0.05}(Ni_{0.25}Fe_{0.25}Mn_{0.5})_{0.95}]O_2$, and (d) cycling performance of the full cell at 0.05 A g^{-1} over 200 cycles.

electrolyte, leading to rapid and continuous sodium ion delivery into internal FeS_2-NCs. In addition, the heteroatoms work as redox-active sites on poly-cyclic carbon structures. Therefore, the high aspect ratio N-rGONRs can diversely affect the overall electrochemical performance of FeS_2-NCs by (1) binding FeS_2-NCs for stable cycling, (2) supplying an electrical conducting pathway and efficient sodium ion delivery, and (3) contributing to the specific capacity.

The electrochemical performance of the FeS_2-NCs/N-rGONRs hybrid anode was tested in an electrolyte of 1 M $NaPF_6$ in DEGDME over the voltage window of 0.01–2.7 V vs. Na^+/Na (Fig. 3). The galvanostatic discharge/charge profiles of the hybrid anode and FeS_2-NCs revealed similar curves, and the profiles changed dramatically after the 1st cycle. The sodium ion storage mechanism of FeS_2-NCs was revealed as two steps [13]:

$$1\ FeS_2 + 2Na^+ + 2e^- \rightarrow Na_2FeS_2$$
$$2\ Na_2FeS_2 + 2Na^+ + 2e^- \rightarrow 2Na_2S + Fe$$

According to the formula, the theoretical capacity of FeS_2 was calculated to be ~894 mA h g^{-1}, and the sodium ion storage reaction occurs via three different phases, such as FeS_2, Na_2FeS_2, and $2Na_2S$. Basically, the voltage profile of an active material via three phases has two different voltage plateaus, which are discontinuous, because the sodium ion storage reaction proceeds sequentially through two different binary phase reactions with different chemical potentials (Fig. S2). In these results, the 1st discharge profile had a voltage plateau at ~1.2 V and a plateau-like section around 0.7 V, indicating the sodium ion storage mechanism based on the three phases (Fig. 3(a)). In contrast, the 1st charge profile exhibited only one voltage plateau at ~1.2 V. The large difference between the discharge and charge profiles suggests that the sodiation pathway is different from the desodiation process. In addition, the plateau at ~1.2 V disappeared in the subsequent discharge process, whereas the charge profiles were similar to the 1st charge profile. A similar tendency during the sodiation/desodiation process of the FeS_2-NCs/N-rGONRs hybrid anode was observed in the cyclic voltammetry (CV) curves tested at a scan rate of 0.01 mV s^{-1} (Fig. 3(b)). The plateau at ~1.2 V in the 1st discharge profile could be induced by sodium intercalation into the FeS_2-NCs lattices to form Na_2FeS_2. The sodiated FeS_2-NCs could suffer from a poor electrical conducting pathway because of the large volume expansion with sodiation. As shown in Fig. 3(c), the rate capability of the FeS_2-NCs anode was insufficient for application, which could be caused by a conversion reaction producing non-conducting Na_2S with large volume expansion. Fig. S3 supports this claim. After sodiation in a FeS_2-NCs anode, the conducting pathway made by carbon black particles (Super P) appears to be fully covered by discharge products, leading to poor rate capabilities. In contrast, the FeS_2-NCs/N-rGONRs hybrid anode could have a well-developed conducting pathway, even after full sodiation, resulting in high rate capabilities in the current range from 0.2 to 10 A g^{-1} (Fig. 3(c)). In the rate cycling tests, the hybrid anodes showed high reversible capacities of ~800 mA h g^{-1} at 0.2 A g^{-1}, which decreased gradually with increasing current rate, and the reversible capacity reached 60% of the initial capacity (480 mA h g^{-1}) at a 50 times higher current rate (10 A g^{-1}) (Fig. 3(b)). The N-rGONRs can provide an electrical pathway for the FeS_2-NCs and thoroughly bind the FeS_2-NCs in repetitive cycling. Therefore, the initial reversible capacities were well-maintained over 200 cycles (Fig. 3(d)), in which an average capacity of ~670 mA h g^{-1} was retained after 200 cycles.

The practicability of FeS_2-NCs/N-rGONRs was demonstrated as a full cell test with an O_3-type ($Na_{0.9}+[Li_{0.05}(Ni_{0.25}Fe_{0.25}Mn_{0.5})_{0.95}]O_2$) cathode. The galvanostatic charge/discharge behaviors of the cathode materials were tested over the voltage range, 2.5–4.2 V (Fig. S4(a)). The cathode showed a reversible capacity of ~140 mA h g^{-1} with a linear voltage profile, of which the mean voltage was calculated to be 3.30 V. In addition, the cathode exhibited good rate capabilities at currents ranging from 50 to 2000 mA g^{-1} and cycling stability over 200 cycles at 50 mA g^{-1} (Fig. S4(b, c)). The FeS_2-NCs/N-rGONRs//($Na_{0.9}+[Li_{0.05}(Ni_{0.25}Fe_{0.25}Mn_{0.5})_{0.95}]O_2$) full cells were prepared using the pre-cycled anode and cathode in the voltage ranges of 0.01–2.5 V and 2.5–4.2 V, respectively (Fig. 4(a)). After pre-cycling, the respective anode and cathode were disassembled from the half cells, and a full cell was prepared using the pre-cycled electrodes and separator used in the anode part. No additional electrolyte and separator were used for the full cell test to minimize the electrolyte contents and reduce the formation of an additional solid electrolyte interface layer. As shown in Fig. 4(a), the full cell was operated over the voltage window of 0.5–4.2 V, of which the capacity balance between both electrodes was controlled by the anode to cathode mass ratio. Galvanostatic charge/discharge profiles of the full cell revealed the characteristic voltage profiles of the anode material in a high voltage level, in which an initial reversible capacity of 102 mA h g^{-1} and average voltage of ~2.67 V were achieved (Fig. 4(b)). The calculated energy densities were ~272 W h kg^{-1} and ~73 W h kg^{-1} at ~126 W kg^{-1} and ~635 W Kg^{-1}, respectively. The energy and power performances were significantly higher than those of other energy storage devices reported (Fig. 4(c)) [30–33]. In addition, the full cell showed remarkable cycling stability for more than 200 cycles with ~75% capacity retention after cycling (Fig. 4(d)). The gradual capacity drop of the full cell could be due to the cathode material. Accumulation of unwanted byproducts originating from electrolyte decomposition and damaged active surfaces can block the reversible redox reaction of cathode materials, leading to the severe capacity imbalance between anode and cathode. Therefore, the cycling stability gradually deteriorated. As shown in ex-situ Fe-SEM image of the cathode materials, it is confirmed that the active surface is fully covered by byproducts after 200 cycles (Fig. S5).

Conclusion

Pyrite FeS_2-NCs with a size of <~100 nm and N-rGONRs were prepared by a solution process, and assembled as a nanohybrid electrode by simple vacuum filtration. In the nanohybrid electrode, the FeS_2-NCs were bound thoroughly by N-rGONR networking, showing high electrochemical performance due to the nanohybrid effects. The FeS_2-NCs/N-GONR nanohybrid anode showed high reversible capacities of ~800 mA h g^{-1} at 0.2 A g^{-1}, and high rate capabilities of ~10 A g^{-1} with a capacity retention of 60% compared to the initial capacity. In addition, sustainable cycling behaviors were achieved after 200 cycles by maintaining average specific capacities of ~670 mA h g^{-1}. In the full cell test with an O_3-type cathode material, the FeS_2-NCs/N-GONR//($Na_{0.9}+[Li_{0.05}(Ni_{0.25}Fe_{0.25}Mn_{0.5})_{0.95}]O_2$) cells exhibited a high specific energy of ~272 W h kg^{-1} at 126 W kg^{-1} and stable cycling for more than 200 cycles. Overall, the nanohybrid anodes have potential for practicable applications.

Acknowledgments

This study was supported by the Basic Science Research Program through the National Research Foundation of Korea (NRF) funded by the Ministry of Education (No. 2017R1C1B1004167), (No. 2019R1A2C1084836) and (No. 2018R1A4A1025169). This study was supported by 2018 Research Grant (PoINT) from Kangwon National University.

Appendix A. Supplementary data

Supplementary material related to this article can be found, in the online version, at doi:https://doi.org/10.1016/j.jiec.2019.08.059.

References

[1] N. Yabuuchi, K. Kubota, M. Dahbi, S. Komaba, Chem. Rev. 114 (2014) 11636.
[2] M.D. Slater, D. Kim, E. Lee, C.S. Johnson, Adv. Funct. Mater. 23 (2013) 947.
[3] S.Y. Cho, M. Kang, J. Choi, M.E. Lee, H.J. Yoon, H.J. Kim, C. Leal, S. Lee, H.-J. Jin, Y.S. Yun, Small 14 (2018)1703043.
[4] Y.S. Yun, Y.-U. Park, S.-J. Chang, B.H. Kim, J. Choi, J. Wang, D. Zhang, P.V. Braun, H.-J. Jin, K. Kang, Carbon 99 (2016) 658.
[5] J.-K. Park, Principles and Applications of Lithium Secondary Batteries, Wiley-VCH Verlag & Co. KGaA, Weinheim, Germany, 2012.
[6] H. Hou, X. Qiu, W. Wei, Y. Zhang, X. Ji, Adv. Energy Mater. 7 (2017)1602898.
[7] D. Su, H.-J. Ahn, G. Wang, Chem. Commun. 49 (2013) 3131.
[8] H. Li, Y. Wang, J. Jiang, Y. Zhang, Y. Peng, J. Zhao, Electrochim. Acta 247 (2017) 851.
[9] N.R. Kim, J. Choi, H.J. Yoon, M.E. Lee, S.U. Son, H.-J. Jin, Y.S. Yun, ACS Sustain. Chem. Eng. 5 (2017) 9802.
[10] J. Choi, N.R. Kim, K. Lim, K. Ku, H.J. Yoon, J.G. Kang, K. Kang, P.V. Braun, H.-J. Jin, Y.S. Yun, Small 13 (2017)1700767.
[11] C. Zhu, P. Kopold, W. Li, P.A. van Aken, J. Maier, Y. Yu, Adv. Sci. 2 (2015)1500200.
[12] Y. Zhu, L. Suo, T. Gao, X. Fan, F. Han, C. Wang, Electrochem. Commun. 54 (2015) 18.
[13] M. Walter, T. Zund, M.V. Kovalenko, Nanoscale 7 (2015) 9158.
[14] Z. Liu, T. Lu, T. Song, X.-Y. Yu, X.W. Lou, U. Paik, Energy Environ. Sci. 10 (2017) 1576.
[15] W. Chen, S. Qi, M. Yu, X. Feng, S. Cui, J. Zhang, L. Mi, Electrochim. Acta 230 (2017) 1.
[16] Y. Kim, Y. Kim, A. Choi, S. Woo, D. Mok, N.-S. Choi, Y.S. Jung, J.H. Ryu, S.M. Oh, K. T. Lee, Adv. Mater. 26 (2016) 4139.
[17] T.H. Vo, M. Shekhirev, D.A. Kunkel, M.D. Morton, E. Berglund, L. Kong, P.M. Wilson, P.A. Dowben, A. Enders, A. Sinitskii, Nat. Commun. 5 (2014) 3189.
[18] J.H. Choe, J. Jeon, M.E. Lee, J.J. Wie, H.-J. Jin, Y.S. Yun, Nanoscale 10 (2018) 2025.
[19] Y.S. Yun, D.-H. Kim, S.J. Hong, M.H. Park, Y.W. Park, B.H. Kim, H.-J. Jin, K. Kang, Nanoscale 7 (2015) 15051.
[20] S.Y. Cho, H.J. Yoon, N.R. Kim, Y.S. Yun, H.-J. Jin, J. Power Sources 329 (2016) 536.
[21] Y.S. Yun, H.-J. Jin, Mater. Lett. 198 (2017) 106.
[22] D.V. Kosynkin, A.L. Higginbotham, A. Sinitskii, J.R. Lomeda, A. Dimiev, B.K. Price, J.M. Tour, Nature 458 (2009) 872.
[23] S. Park, Y. Hu, J.O. Hwang, E.-S. Lee, L.B. Casabianca, W. Cai, J.R. Potts, H.-W. Ha, S. Chen, J. Oh, S.O. Kim, Y.-H. Kim, Y. Ishii, R.S. Ruoff, Nat. Commun. 3 (2012) 638.
[24] Y.S. Yun, K.-Y. Park, B. Lee, S.Y. Cho, Y.-U. Park, S.J. Hong, B.H. Kim, H. Gwon, H. Kim, S. Lee, Y.W. Park, H.-J. Jin, K. Kang, Adv. Mater. 27 (2015) 6914.
[25] Y.S. Yun, J.M. Kim, H.H. Park, J. Lee, Y.S. Huh, H.-J. Jin, J. Power Sources 244 (2013) 747.
[26] M.Y. Song, Y.S. Yun, N.R. Kim, H.-J. Jin, RSC Adv. 6 (2016) 19389.
[27] Y.S. Yun, Y.H. Bae, D.H. Kim, J.Y. Lee, I.-J. Chin, H.-J. Jin, Carbon 49 (2011) 3553.
[28] S.Y. Cho, Y.S. Yun, D. Jang, J.W. Jeon, B.H. Kim, S. Lee, H.-J. Jin, Nat. Commun. 8 (2017) 74.
[29] S.Y. Cho, Y.S. Yun, S. Lee, D. Jang, K.-Y. Park, J.K. Kim, B.H. Kim, D.L. Kaplan, H.-J. Jin, Nat. Commun. 6 (2015) 7145.
[30] E. Lim, C. Jo, M.S. Kim, M.-H. Kim, J. Chun, H. Kim, J. Park, K.C. Roh, K. Kang, S. Yoon, J. Lee, Adv. Funct. Mater. 26 (2016) 3711.
[31] M.S. Kim, E. Lim, S. Kim, C. Jo, J. Chun, J. Lee, Adv. Funct. Mater. 27 (2017) 1603921.
[32] Z. Le, F. Liu, P. Nie, X. Li, X. Liu, Z. Bian, G. Chen, H.B. Wu, Y. Lu, ACS Nano 11 (2017) 2952.
[33] Y. Long, J. Yang, X. Gao, X. Xu, W. Fan, J. Yang, S. Hou, Y. Qian, ACS Appl. Mater. Interfaces 10 (2018) 10945.